Merged and Gridded GPM and Atmospheric River Data Product

Marian E. Mateling[1], Claire Pettersen[2], Kyle Mattingly[3], and Sarah Ringerud[4]

[1] Department of Atmospheric and Oceanic Sciences, University of Wisconsin-Madison, Madison, WI, USA
[2] Climate and Space Sciences and Engineering, University of Michigan-Ann Arbor, Ann Arbor, MI, USA
[3] Space Science and Engineering Center, University of Wisconsin–Madison, Madison, WI, USA
[4] NASA's Goddard Space Flight Center, Greenbelt, MD 20771, USA

Corresponding author: Marian Mateling (mateling@wisc.edu)

Key Points

- A new dataset is presented that collocates satellite-derived precipitation rates and water vapor with reanalysis-derived atmospheric rivers
- Higher precipitation rates and water vapor content are coincident with atmospheric river events in the high-latitude regions
- An example application illustrates warmer, more moist conditions during precipitating AR events that are present in the GPROF database

Abstract

The Global Precipitation Measurement (GPM) Mission Core Observatory satellite launched in 2014 as a joint mission between NASA and JAXA. GPM has, since that time, provided continuous, valuable dual-frequency radar and passive microwave radiometer observations. Here, we introduce a gridded dataset of collocated GPM Core Observatory observational products merged with a reanalysis-derived atmospheric river dataset in the North Atlantic and North Pacific sectors. The three datasets that are merged and gridded are: a) the NASA Goddard Profiling (GPROF) precipitation product, which uses GPM passive microwave radiometer observations to derive surface precipitation rates, b) a water vapor data product derived from the GPM Core Observatory radiometer, provided by Remote Sensing Systems (RSS), and c) the Mattingly et al. (2018) atmospheric river dataset that is specifically tuned to the high-latitude regions. This novel merged dataset spans from May 2014 to December 2022 with plans to update annually through 2026 at minimum. This gridded product combines RSS passive water vapor and precipitation estimates with coincident atmospheric river detection. This data product benefits the scientific community by providing (a) user-friendly gridded satellite data compared to standard satellite datasets, while maintaining high temporal resolution, and (b) coincident satellite observations to assess the link between atmospheric rivers and precipitation.

Plain Language Summary

This paper summarizes the creation of a new, gridded dataset containing precipitation, atmospheric water vapor content, and atmospheric river information from May 2014 to December 2022. The precipitation and water vapor data are both remotely-sensed data products using the Global Precipitation Measurement (GPM) Core Observatory Microwave Imager (GMI). The atmospheric river algorithm detection is more sensitive to moisture transport than global algorithms and is thus better suited to colder and drier environments. We temporally match and interpolate all data to a common grid and provide examples of the merged data to illustrate the seasonality and impacts of atmospheric river presence on precipitation. Lastly, we demonstrate the utility of this dataset by investigating the assumptions used to estimate precipitation from GMI measurements. The dataset confirms that atmospheric rivers are associated with warmer temperatures, higher water vapor content, and more intense precipitation rates.

1 Introduction

The transport of water vapor through the atmosphere is tied to the intensity and phase of precipitation around the world, and more recently has been used in forecasting the severity of precipitation events (Baggett et al., 2017; Ralph et al., 2020). Atmospheric rivers (ARs) are long, narrow features of relatively high integrated water vapor transport (IVT; atmospheric water vapor flux through a vertical column) that evolve with atmospheric circulation (Zhu & Newell, 1998; Gimeno et al., 2014; Guan & Waliser, 2015; Ralph et al., 2018). Recent work has investigated the links between model-derived ARs and precipitation over land and coastal topography (e.g., Guan et al., 2010; Slinskey et al., 2020; Cann & Friedrich, 2020; Prein & Heymsfield, 2020; Mateling et al., 2021). Few studies of ARs include satellite data due, in part, to AR algorithms relying on the complete spatio-temporal coverage of gridded model datasets, in contrast with the often-inconsistent spatio-temporal data observed by satellites (e.g., Ralph et al., 2004). Recently, spaceborne radar retrievals from the Global Precipitation Measurement (GPM) Core Observatory have illustrated the use of satellite remote sensing observations to study AR impacts on precipitation at select locations (e.g., the western U.S. coast; Cannon et al., 2017; Cannon et al., 2020), but these studies have generally focused on the mid-latitude regions. Here, we provide a merged dataset of GPM Core Observatory precipitation and water vapor products with ARs in the North Atlantic and North Pacific sectors. The goal of this product is to encourage further exploration of high-latitude ARs and their impact on precipitation estimates from spaceborne microwave radiometer observations.

AR data products, derived from model and reanalysis data, generally vary in criteria for IVT magnitude, anomalies, and geometry in identifying ARs (Shields et al., 2018). Recent studies show that the magnitude and size of ARs are correlated to the intensity, phase, and location of

precipitation around the world (Guan & Waliser, 2015; Mattingly et al., 2016; Ma et al., 2020). More specifically, the incidence of ARs leads to higher precipitation rates (Guan et al., 2010; Lavers & Villarini, 2013; Cann & Friedrich, 2020), and increased likelihood of precipitation being liquid versus frozen (Guan et al., 2016; Goldenson et al., 2018; Mateling et al., 2021). In Mattingly et al. (2018), the authors created an algorithm that identifies ARs in relatively cold and dry atmospheric conditions (high latitudes). Researchers use this Mattingly et al. (2018) AR scheme (hereafter, "M18") to study AR impacts on Greenland Ice Sheet surface mass balance (M18; Mattingly et al., 2020; Mattingly et al., 2023) and Upper Great Lakes precipitation (Mateling et al., 2021).

The GPM Core Observatory (GPM-CO) is a low-earth orbiting satellite that is part of a joint mission by NASA (National Aeronautics and Space Administration) and JAXA (Japanese Aerospace and Exploration Agency) launched in March 2014 and has since provided valuable data from its onboard dual-frequency radar and passive microwave radiometer (Hou et al., 2014; Skofronick-Jackson et al., 2017; Skofronick-Jackson et al., 2018). The GPM Microwave Imager (GMI) has 13 passive microwave channels (10-183 GHz) and obtains brightness temperatures at the top of the atmosphere (Draper et al., 2015). The Goddard Profiling Algorithm (GPROF) is the operational passive microwave algorithm for GMI and retrieves surface precipitation rate and phase (Kummerow et al., 2015; Randel et al., 2020).

Also using GMI observations Remote Sensing Systems (RSS) created a daily integrated atmospheric water vapor product (as well as other data; Meissner et al., 2012). The incidence of M18 ARs, defined by IVT, and GMI-retrieved water vapor can be used to diagnose or evaluate methods used to identify the location, shape, and size of ARs. Further, coincident GPROF precipitation estimates provide insight into how the presence of high-latitude ARs impact observed precipitation rates and phase.

Here we present a gridded and merged dataset that includes the M18 ARs, precipitation estimates from GMI GPROF, and the GMI-derived atmospheric water vapor. This dataset is intended to be a comprehensive, satellite-based tool for the broader scientific community with the aim of investigating ARs and high-latitude precipitation over the North Atlantic and Pacific regions. In section 2, we detail the GMI data products and the AR scheme. Section 3 outlines the gridding and merging process for the combined dataset. Section 4 illustrates examples from the dataset during boreal summer (June-July-August, JJA) and winter (December-January-February, DJF). In section 5, we demonstrate an application of the merged dataset.

2 Datasets used in Merged Product

The three distinct datasets merged are the GPM GMI GPROF VERSION 07 (V7) precipitation product, the RSS GMI-derived atmospheric water vapor product, and high-latitude ARs derived

by Mattingly et al. (2018) using the Modern-Era Retrospective analysis for Research and Applications Reanalysis, Version 2 (MERRA-2; Gelaro et al., 2017). We grid the spatio-temporally irregular GMI GPROF V7 to a common 0.25° × 0.25° grid for the merged product to match the already-gridded RSS water vapor product. For this initial version of the database, we opted to use the North Atlantic boundaries of: 45 - 70° N, 70° W - 10° E, and the North Pacific boundaries of: 45 - 70° N, 140° E - 120° W. Both sectors are latitudinally limited by the GPM-CO orbital inclination, 65° N, but we extended the domain up to 70° N as GMI observes brightness temperatures at latitudes up to ~69° N. The database covers the time period from May 2014 to December 2022, beginning shortly after the GPM-CO launch date in March 2014, and will be updated annually. Files are provided for each basin and each month in network Common Data Form (NetCDF-4) file format. See Appendix A for a full list of each netCDF-4 file's contents.

Two of the three datasets in this merged product are derived from the GPM-CO microwave radiometer (GMI). Though the GPROF algorithm is applied to several other spaceborne microwave radiometer observations, GMI is the best calibrated. This multi-channel dual-polarization radiometer has a swath width of 885 km, observing at higher latitudes (~|69|°) than the limit of the GPM-CO orbit (|65|°). Additionally, the GPM-CO has a high return-rate at high latitudes (~|60|°) due to orbital inclination.

2.1 GPROF Data

The GMI GPROF V07 precipitation product is provided by the NASA Goddard Earth Sciences (GES) Data and Information Services Center (DISC; Kummerow, 2022). The GPROF algorithm is a Bayesian scheme applied to GMI observations to estimate precipitation rate (Kummerow et al., 2015; Randel et al., 2020). The GMI-only version of GPROF (GPM_2AGPROFGPMGMI) included in the merged product uses the observed brightness temperature vector from GMI to search a pre-existing, or *a priori*, database containing one year of matched GPM-CO observations with atmospheric information. This Bayesian scheme then retrieves a hydrometeor profile used to estimate precipitation rate. This database was created using the GPM Combined Algorithm (Grecu et al., 2016) which retrieves the optimal precipitation profile based upon the dual-frequency radar reflectivity values (from the GPM Dual-frequency Precipitation Radar, or DPR) and multi-frequency brightness temperatures.

The nearrealtime GPROF algorithm searches the *a priori* database using the observed GMI brightness temperature vector and is constrained using Japanese Global Analysis (GANAL) two-meter temperature (T2M), total precipitable water (TPW), and surface type (Randel et al., 2020). GPROF determines precipitation phase using ancillary surface wet bulb temperature and pre-defined lookup tables (Sims & Liu, 2015) which allows separation of liquid (rain) and frozen precipitation rates. We include both total and frozen precipitation rates in this merged dataset.

GMI GPROF underperforms when determining light or frozen precipitation due to the lack of DPR reflectivities ≤ 12 dBZ within the *a priori* database (Skofronick-Jackson et al., 2019). For a full explanation of the GPROF V7 algorithm, see Randel et al. (2020) or the Algorithm Theoretical Basis Document (ATBD; Passive Microwave Algorithm Team Facility, 2022). Variables obtained and gridded from the GMI GPROF V7 product include surface precipitation rates (liquid plus frozen precipitation), frozen precipitation rates, T2M, and the surface type flag (land, ocean, mixed). The GPROF product footprint resolution is 18.1 km × 10.9 km and defined at the center of the GMI footprint. All precipitation rates presented are liquid water equivalent (LWE).

2.2 RSS Water Vapor Data

We additionally merge the atmospheric water vapor from GMI observations created by the Remote Sensing Systems (RSS) group. To derive this product, GMI passive microwave data (obtained through GES DISC) are back-processed and put through the RSS Version-8.2 algorithm to derive brightness temperature. The RSS radiative transfer model then uses these brightness temperatures to retrieve the total column water vapor (Wentz et al., 2015; Meissner et al., 2012). We downloaded daily averages of water vapor from May 2014 - December 2022 at 0.25° × 0.25° spatial resolution from the RSS website (see data availability section). Provided are two files per day, for ascending and descending GPM-CO orbital tracks, with time steps given in fractional hours per day. The temporal resolution is either a daily average of water vapor or as the most recent value of water vapor, overwriting derived water vapor from a preceding overpass on the same day. The water vapor is not computed over land or near coastlines as these surface types can complicate the GMI observations and create large uncertainties (Meissner et al., 2012). More detailed information on the derivation of water vapor from GMI data can be found in the product's ATBD (Meissner et al., 2012).

2.3 Atmospheric Rivers

The final component of the merged dataset is the inclusion of ARs as defined in M18. M18 uses 6-hourly MERRA-2 wind and specific humidity data between 1000 and 200 hPa to compute integrated water vapor transport (IVT) in kg m^{-1} s^{-1}, which is then re-gridded to 0.5° × 0.5°. IVT is composed of the total water vapor summed throughout the column multiplied by the winds that are transporting it:

$$IVT = \frac{1}{g}\int_{1000\,hPa}^{200\,hPa} qV\,dp\,,$$

where g is gravitational acceleration, q is specific humidity, V is vector wind, and dp is the difference between pressure levels. The RSS water vapor data directly relates to the moisture component of the IVT equation but is from GMI rather than the MERRA-2 reanalysis that is used to calculate IVT for AR identification. An AR is identified when IVT exceeds both a

minimum absolute threshold of 150 kg m^{-1} s^{-1} and the 85th percentile of the grid-cell-specific 31-day centered climatology, with potential AR objects further filtered by geometric criteria: (a) length of 1500 km and (b) a length-to-width ratio of 1.5 (M18). This AR dataset was developed with the intention of identifying the size and location of ARs in the high-latitude regions where atmospheric moisture is relatively low, requiring a more sensitive detection threshold of IVT than many other AR algorithms (e.g., Rutz et al., 2019). Additionally, if the AR object center is poleward of |70|°, the algorithm does not require the IVT direction to be poleward like most other AR algorithms. This may slightly increase the number of GPM-AR intersections at the northern edge of the study domain, particularly during summer (JJA).

3 Merged AR-GPM Gridded Product

3.1 Methodology

Merging the GPM-CO data products, which have irregular, but high-resolution spatial and temporal coverage, with a spatially-gridded, 6-hourly temporal resolution M18 AR dataset requires additional steps to best match the respective product information. We chose a 0.25° × 0.25° (latitude × longitude) spatial grid for the merged dataset to match the already-gridded RSS water vapor product and to best maintain the high spatial resolution of the GMI GPROF product. See Table 1 for spatial and temporal resolution of these data products and the merged dataset. The merged data are output into monthly files where each time step represents a GPM-CO overpass through the predefined (North Atlantic or Pacific) basin. The data structure is 3-dimensional (time step by latitude by longitude), with each monthly file containing ~250 time steps.

Dataset	Spatial resolution	Temporal resolution	Reference
M18 Atmospheric Rivers	0.5° × 0.5°	6-hourly	Mattingly et al. 2018 (M18)
GPM_2AGPROF GPMGMI V07 precipitation	GMI 19GHz Channel Footprint (18.1 km × 10.9 km)	Instantaneous < 1 min	ATBD (Passive Microwave Algorithm Team Facility, 2022)
RSS GMI atmospheric water vapor content v8.2	0.25° × 0.25°	Daily averages (ascending and descending)	Wentz et al. 2015 Meissner et al. 2012
Merged GPM-AR Dataset	0.25° × 0.25°	One timestep = one GPM-CO overpass	Appendix A https://doi.org/10.7302

		through basin	/7t62-s085

Table 1: Resolution of the three original datasets and the merged dataset, including references for the datasets.

To grid GMI GPROF data, we pre-define a latitude-by-longitude grid where each gridbox is defined by its lower left corner latitude and longitude. We apply the GMI GPROF product quality flags (L1CqualityFlag = 0, qualityFlag = 0, pixelStatus = 0) that are often applied over land due to radio frequency interference. For each individual GPM-CO overpass file, we aggregate all GMI GPROF precipitation observations that fall within each 0.25° × 0.25° gridbox. Each gridbox contains the conditional mean of precipitation rates ≥ 0.01 mm h^{-1} LWE. We identify the start and end times of each overpass through the basin and find the median time; this is then assigned as the date and time for the gridded overpass. The number of GMI footprints that fall within each grid box while gridding the data is saved as "count" variables to provide sampling data to users. We create a gridded surface flag variable from the footprint-resolution GMI GPROF V7 surface flag by setting grid boxes with 100% ocean footprints as '0' (or ocean surface). Grid boxes that contain footprints flagged as 100% land are assigned a flag of '2' (or land surface). Any grid boxes that contain a combination of ocean and other surface types (which includes sea ice and coastlines) are flagged as '1' (or mixed surfaces).

The RSS water vapor product, derived from GMI brightness temperature observations, is already spatially gridded to 0.25° × 0.25°. Atmospheric water vapor data are daily averages for both the ascending and descending portions of GPM-CO's daily orbit separately. We match these data to individual swaths of GMI GPROF data by converting the given fractional hour information and identifying the associated overpass within GMI GPROF timesteps.

Finally, to merge the M18 AR data, we split the 0.5°× 0.5° grid boxes into 0.25°×0.25° to match the RSS water vapor and now-gridded GMI GPROF V7 data. Next, we find the midpoint of each GPM-CO overpass through the basin (either North Atlantic or Pacific) and identify the nearest 6-hourly timestep defined in the M18 AR dataset (00, 06, 12, and 18 UTC). By matching the spatio-temporal resolution between these datasets, we are able to analyze satellite precipitation products during AR events (or precipitation when no AR is present, or "No AR" events). We have eliminated AR data outside the GMI swaths to remain a GMI-based merged dataset, though the M18 dataset encompasses the Northern Hemisphere at latitudes ≥10°N.

Notably, for the remainder of this paper, we only show the merged data product over ocean surfaces (where the gridded surface flag is '0'), where ARs are more frequent and intense due to the availability of water (Guan & Waliser, 2015). Additionally, this remains consistent with the available observations from the RSS water vapor product, and avoids any biases introduced by ground clutter contamination or impacts from coastlines in the GMI observations. Though not included here, the merged product does contain the available gridded GMI GPROF and M18 AR

data over land and "mixed" (coastline or sea ice) surfaces that fall within the specified basin. The lack of surface observations over the North Atlantic and Pacific Oceans complicates validating AR algorithms over-ocean and studying AR impacts on meteorology. The perspective of spaceborne instrumentation is thus a bridge between reanalysis and satellite observations to study high-latitude ARs and precipitation over ocean. See Appendix A for the outline of variable names within the merged dataset that are used in the following figures.

3.2 Example Gridded Output

An example of the pre- and post-gridded RSS daily mean water vapor and GMI GPROF V7 precipitation rates is shown in Figure 1. This GPM-CO overpass, at ~0700 UTC on December 23, 2016, preceded an extreme precipitation event. Fig. 1a shows the RSS ascending daily mean atmospheric water vapor obtained from the RSS website at 0.25° × 0.25° spatial resolution. Fig. 1c- show the GMI GPROF precipitation estimates obtained through the GES DISC at the original GMI footprint resolution. M18 ARs are designated by the contour at 0.5° spatial resolution. The post-gridded and merged water vapor (Fig. 1b), GMI GPROF precipitation (Fig. 1d), and M18 AR (contours) are the data available in the merged dataset. As noted above, we mask data over coastlines and land surfaces for these figures, though the data are available in the merged dataset. The merged data shown in Fig. 1b, d can be recreated using the time step '2016-12-23 07:25:00' in the file name gridded_atlantic_201612.nc in the provided product. Notably, the merged data (Fig. 1b, d) maintain similar features to the original resolution for all three data products (e.g., high water vapor and precipitation rates along the meridional length of the AR). The discontinuity in the RSS water vapor product (Fig. 1a-b) west of Norway that is not present in the GMI GPROF precipitation (Fig. 1c-d) can be attributed to the difference in the original data resolution between the RSS water vapor (daily means of ascending or descending water vapor) and GMI GPROF (individual swaths).

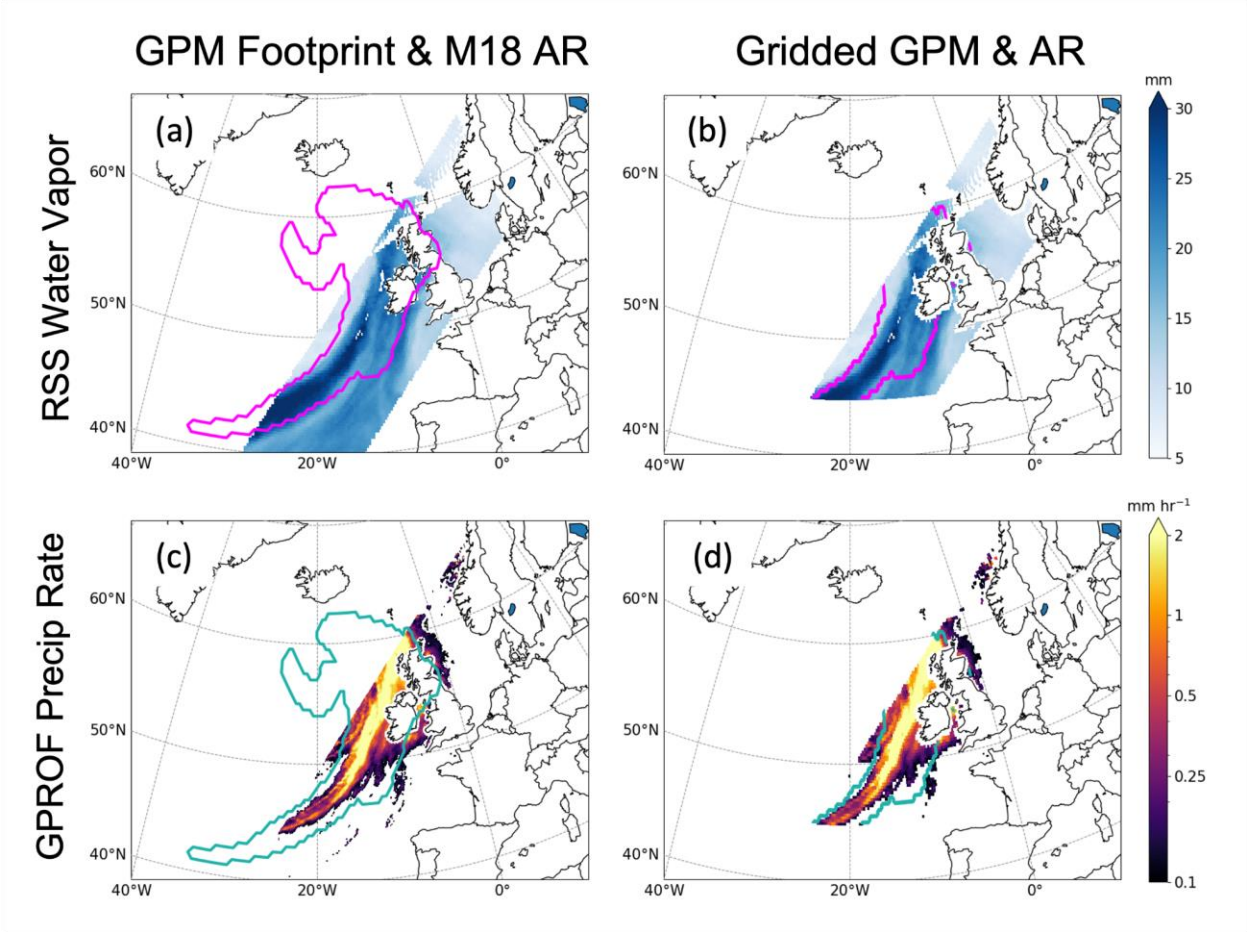

Figure 1: An example of RSS water vapor (a, b) and GMI GPROF precipitation estimates (c, d) during one time step (an ascending overpass) on December 23, 2016. The matched M18 AR is outlined in magenta (top row) and teal (bottom row). All data are shown before gridding (a, c) and after gridding for the merged dataset (b, d). Before gridding, GMI GPROF precipitation data are at GMI footprint resolution. The original gridded resolution of the RSS water vapor and M18 AR data is 0.25° × 0.25° and 0.5° × 0.5°, respectively. The merged dataset resolution for all data is 0.25° × 0.25°. Fig. 1b, d are created using the variables "AR_flag," "surface_precip," and "RSS_wv" in the merged dataset.

Figure 2 shows the counts of GMI footprints collected per 0.25° × 0.25° grid box for the North (a) Atlantic and (b) Pacific for January - December 2016 over ocean only. There is a sharp meridional gradient of footprints with maximum concentration at ~61°N due to the satellite orbital inclination. This maximum is lower in the North Pacific than the North Atlantic, due to the presence of sea ice at ~60°N, and subsequent masking of observations over land / ice. Though we do not include data over land or sea ice in this paper, data for all surface types are

available in the merged dataset netCDFs.

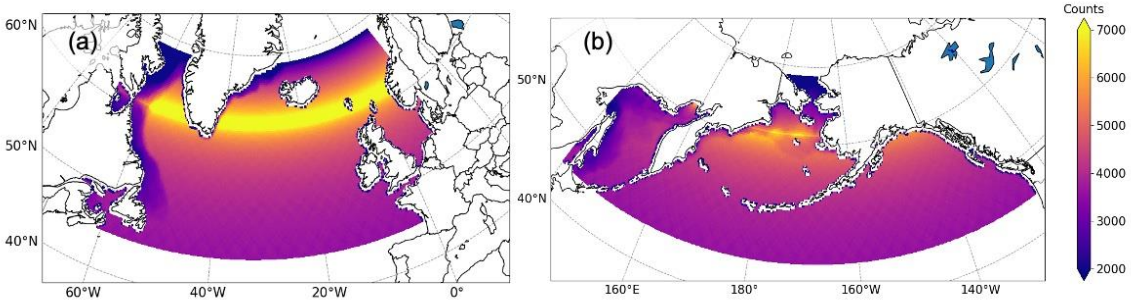

Figure 2: Cumulative number of GMI footprints (ice- and land-free), January - December 2016 per 0.25° × 0.25° grid box for the North (a) Atlantic and (b) Pacific. This figure is created using the variable "opass_counts" in the merged dataset.

Figure 3 shows the composite frequency of the M18 ARs coincident with available GMI footprints in DJF (Fig. 3 a-b) and JJA (Fig. 3 c-d). In DJF (Fig. 3a-b). M18 AR frequency is < 10% in the western (northwestern) portion of the North Pacific (Atlantic), but M18 AR > 10% along and to the east of the storm tracks (southwest to northeast; Blackmon, 1976; Hoskins & Valdes, 1990; Hoskins & Hodges, 2019a; Hoskins & Hodges, 2019b). Literature has identified these eastward and poleward tracks as locations of AR frequency maxima (Zhu & Newell, 1998; Guan & Waliser, 2015). This indicates that the GPM-CO has high enough spatio-temporal coverage to reasonably represent seasonal frequency of ARs. In JJA (Fig. 3c-d), M18 ARs occur more frequently (>10% of the time) in both the North Atlantic and North Pacific basins. Unlike the zonal contrast of AR frequency in DJF, there is little variation in frequency across both basins in JJA. The highest frequencies (>15%) in JJA are in the southeast North Pacific basin, south of the Kamchatka Peninsula, and just east of Baffin Island.

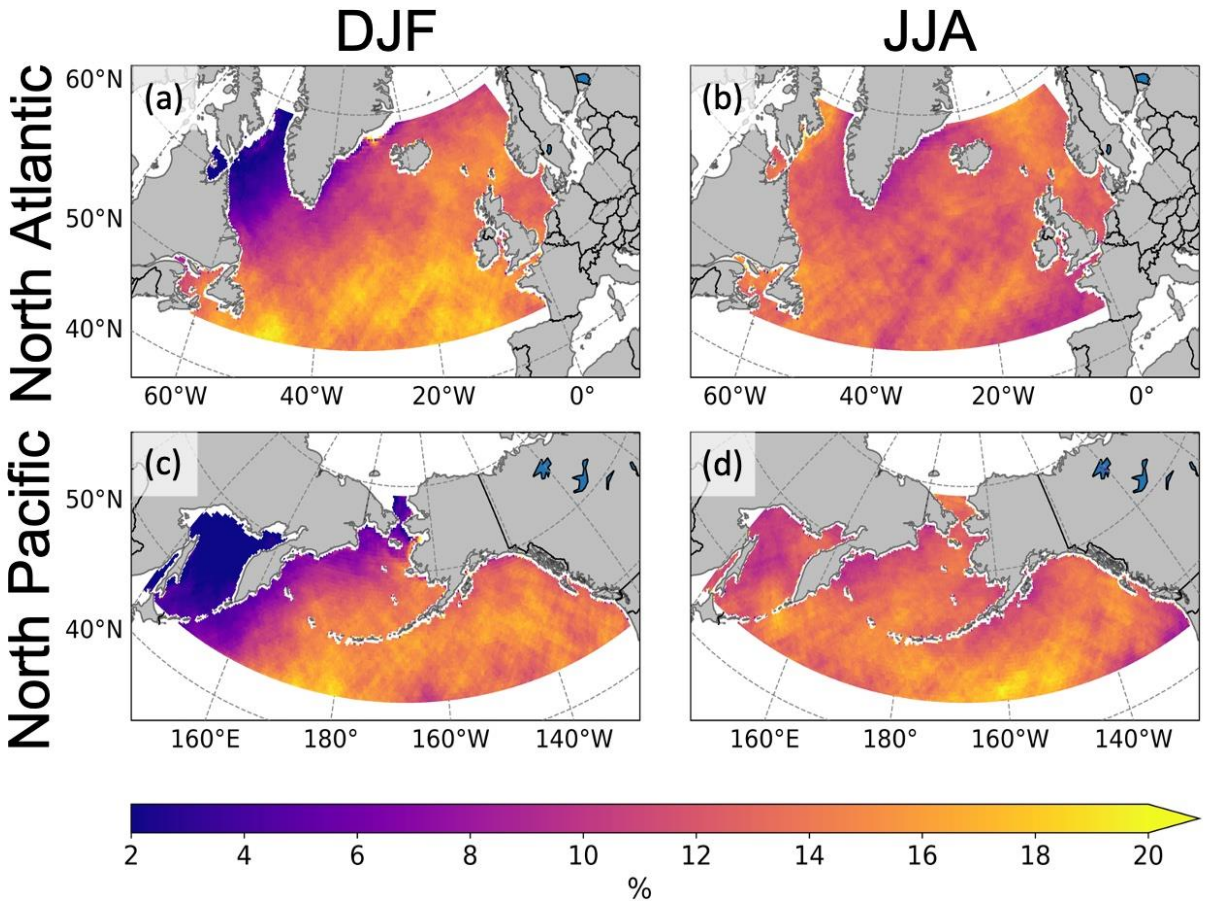

Figure 3: Frequency of atmospheric rivers in (a, c) DJF and (b, d) JJA coincident with GMI footprints (May 2014-December 2022). Frequency is normalized by the total number of GMI footprints per season regardless of precipitation observations. This figure is created using the variable "AR_flag" and is normalized using "opass_counts" shown in Figure 2.

3.3 ERA5

To show an application of the merged dataset, we also utilize hourly, gridded (0.25° × 0.25°) T2M and total column water vapor (another term for TPW) data products from the ECMWF Reanalysis v5 (ERA5; Hersbach et al., 2020). The spatial resolution of ERA5 matches that of the merged dataset (0.25°×0.25°). To match hourly ERA5 data to the irregular timesteps within the gridded dataset, we pair the nearest-time ERA5 timestep and location to the corresponding timestep and location in the merged dataset (i.e., the median times of each overpass through the basin at specific grid points). T2M and TPW are two of the ancillary meteorological variables used to estimate precipitation rates in the GMI GPROF algorithm. We then use the gridded AR flag to examine the meteorological (T2M and TPW) differences based on coincident M18 ARs (see details in Section 5).

4 Examples of Merged Data

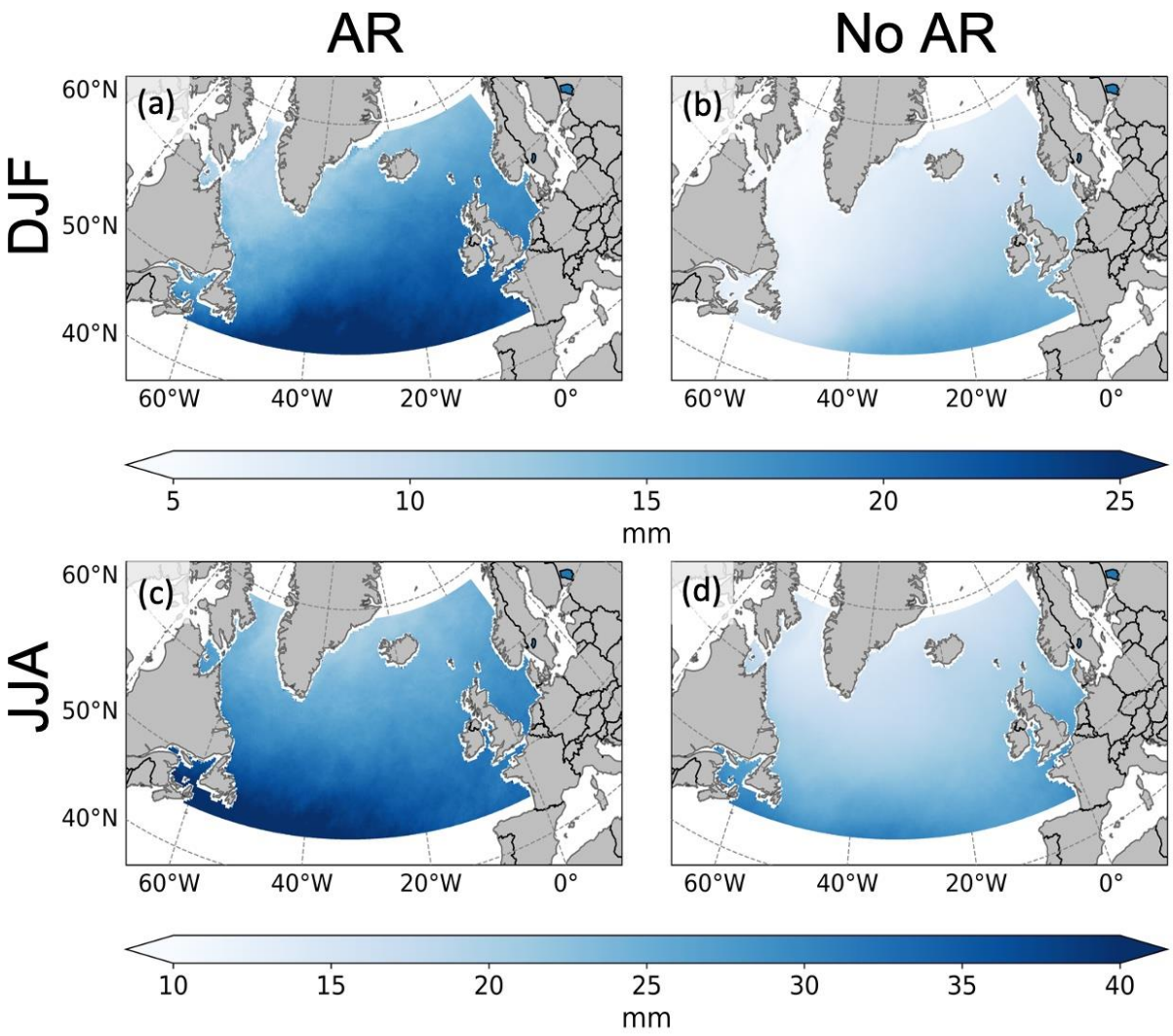

Figure 4: Merged, gridded seasonal averages (May 2014-December 2022) of the daily mean atmospheric water vapor in (a, b) DJF and (c, d) JJA in the North Atlantic during AR and No AR events. Water vapor data are originally from the RSS and derived from GMI data. This figure is created using the variables "AR_flag" and "RSS_wv."

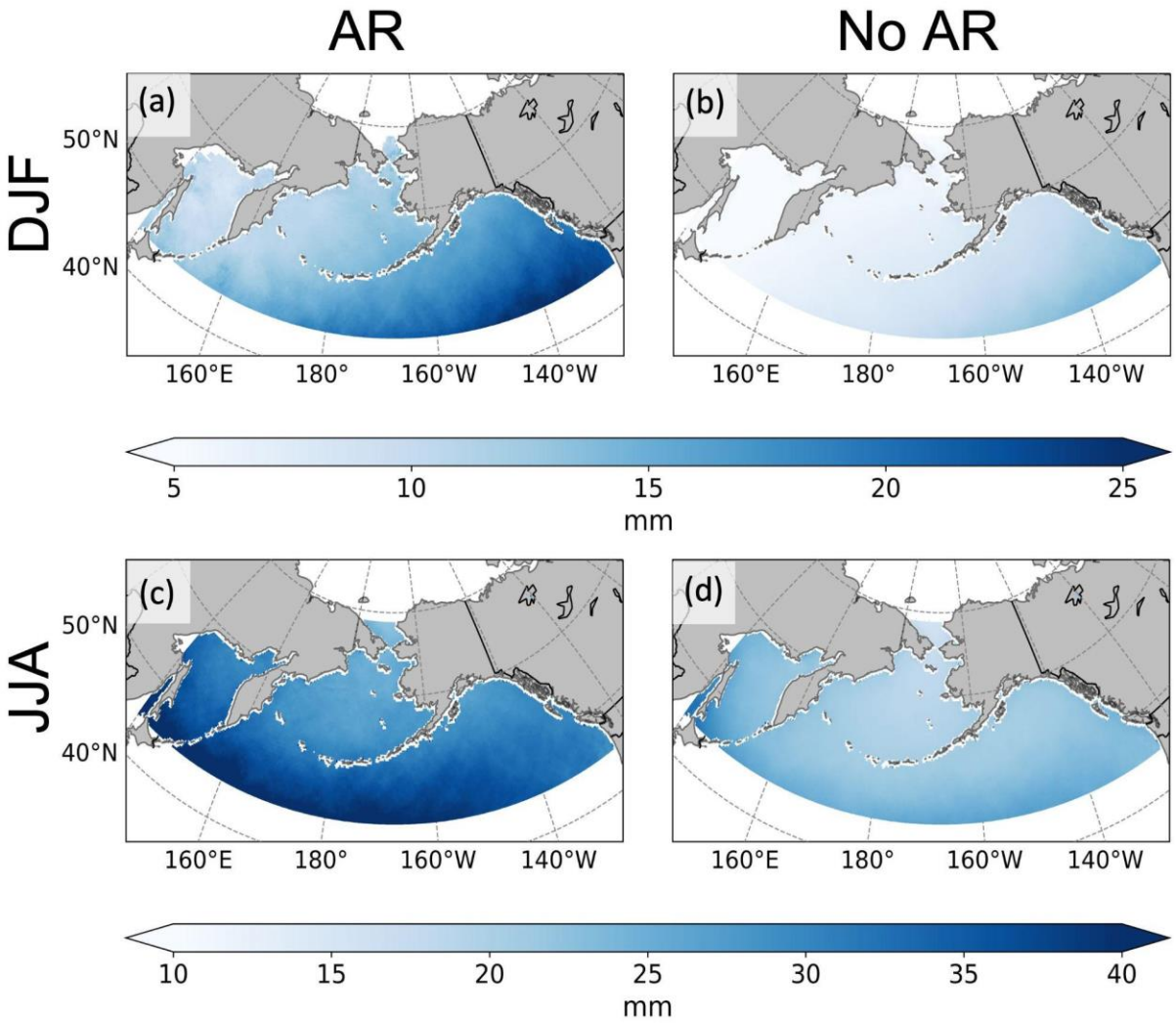

Figure 5: Merged, gridded seasonal averages (May 2014-December 2022) of the daily mean atmospheric water vapor in (a-b) DJF and (c-d) JJA in the North Pacific during AR and no AR events. Water vapor data are originally from the RSS and derived from GMI data. This figure is created using the variables "AR_flag" and "RSS_wv."

Figures 4 and 5 show the gridded mean RSS water vapor for DJF and JJA in the North Atlantic and North Pacific, respectively. These composites are created using the variables "RSS_wv" and "AR_flag" in the merged dataset. Noting the different colorbar scales, the mean water vapor is generally higher in JJA (Fig. 4c-d and Fig. 5c-d) than in DJF (Fig. 4a-b and Fig. 5a–b) for both basins. Additionally, there is higher mean water vapor when an M18 AR is present (Fig. 4a, c and Fig. 5a, c). This is expected given that existing AR detection schemes include percentile analyses of integrated water vapor (Ralph et al. 2018), however it has not been before illustrated with satellite-based observations of water vapor. Inversely, when no M18 AR is present, mean water vapor content is much lower as a function of the respective season (Fig. 4b, d and Fig. 5b,

d). Regions of relatively high mean water vapor in the basins during ARs (Fig. 4a, c and Fig. 5a, c) coincide with high AR frequency (see Fig. 3): along storm tracks and in the southeast basin during DJF (Fig. 3a, c) and basin-wide in JJA (Fig. 3b, d). This result is expected, and indicates that the RSS water vapor product, independent of the M18 AR dataset, is capable of representing meteorological conditions during AR and no AR events.

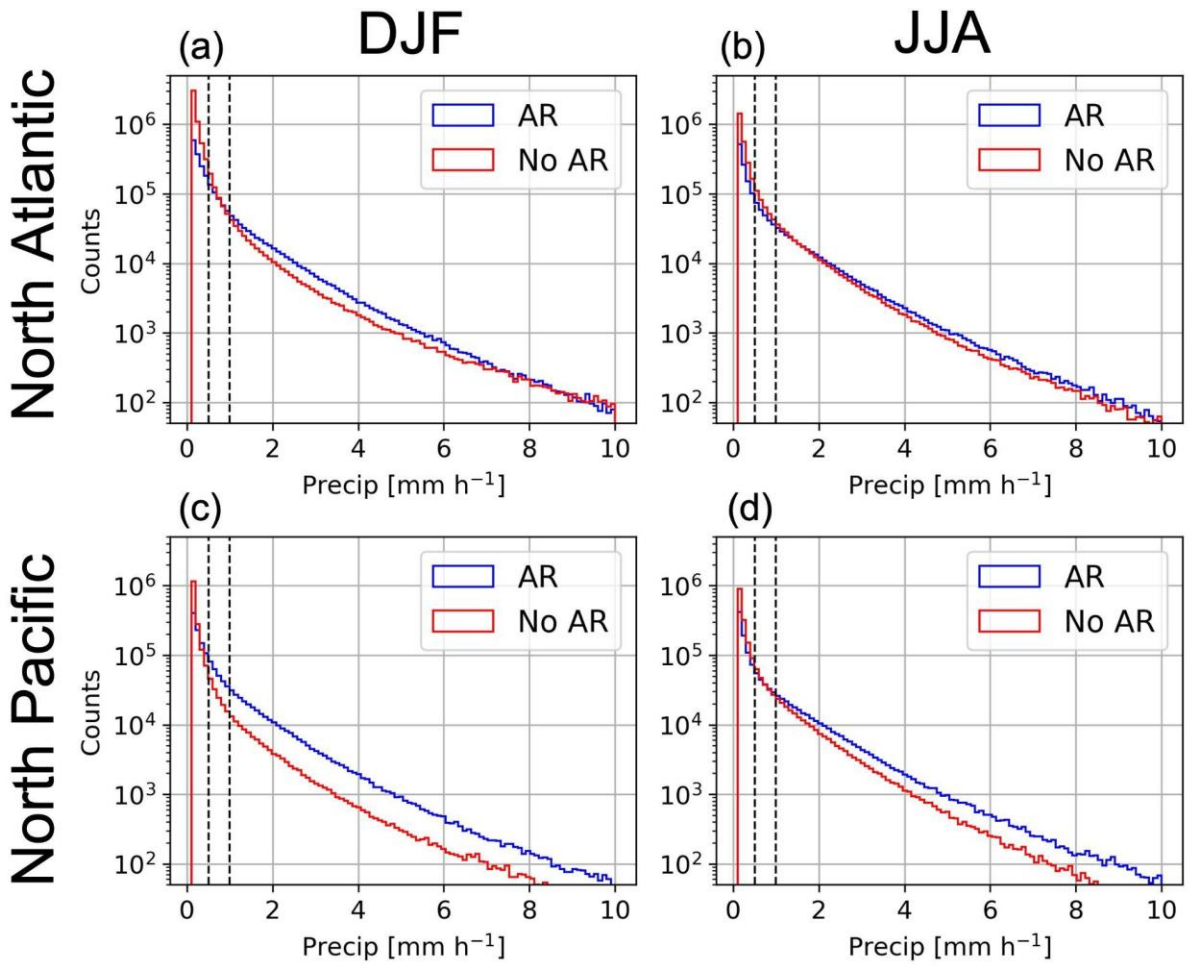

Figure 6: Histograms of gridded GMI GPROF V7 precipitation rates in the (a-b) North Atlantic and (c-d) North Pacific from May 2014 to December 2022. Precipitation rates are categorized as coincident with an M18 AR (blue line) or not (red line) present. Vertical dashed lines are at 0.5 and 1.0 mm h^{-1} LWE for reference. This figure is created using the variables "AR_flag" and "surface_precip" in the merged dataset.

We bin the gridded GMI GPROF V7 precipitation rates (LWE) in Figure 6 seasonally and by basin, with the blue (red) line representing M18 AR (no AR) coincidence. The dashed lines at 0.5 and 1.0 mm h^{-1} LWE represent thresholds used for additional variables in the merged dataset (see Section 6). There is little difference in the amount of precipitation or the frequency of AR-coincident precipitation between DJF (Fig. 6a, c) and JJA (Fig. 6b, d). Precipitation in the North

Atlantic (Fig. 6a-b) is more frequent than in the North Pacific (Fig. 6c-d). Instances of higher precipitation rates in the North Pacific are most likely coincident with an AR (> 0.5 mm h^{-1} in DJF, > 1.0 mm h^{-1} in JJA; Fig. 6c-d). In the North Atlantic, ARs are present for approximately half of precipitation occurrences (Fig. 6a-b). In all cases, most occurrences of light precipitation are not coincident with AR.

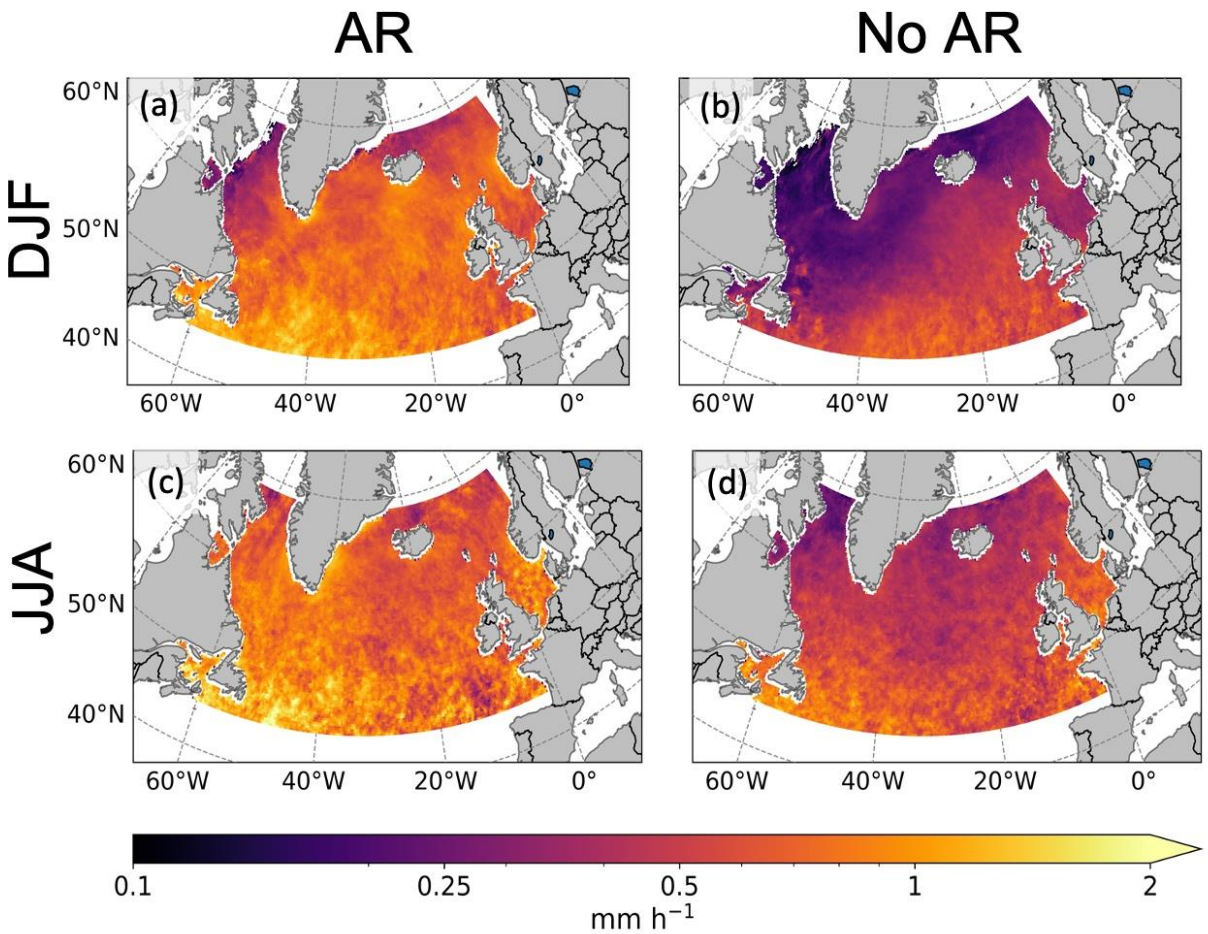

Figure 7: Seasonal conditional mean (≥ 0.1 mm h^{-1} LWE) GMI GPROF precipitation rates (May 2014-December 2022) in (a-b) DJF and (c-d) JJA during AR and No AR events in the North Atlantic. This figure is created using the variables "AR_flag" and "surface_precip" in the merged dataset.

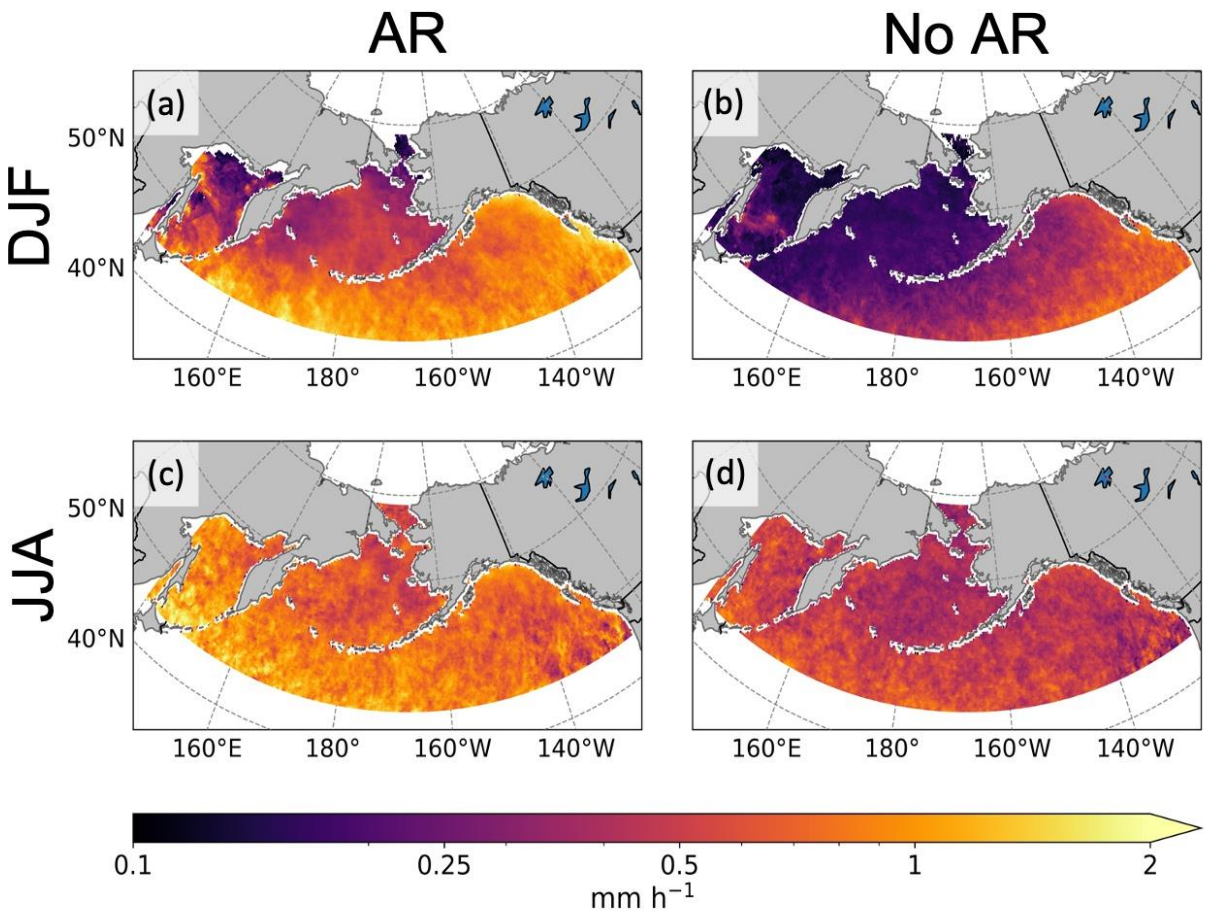

Figure 8: Seasonal conditional mean (≥ 0.1 mm h^{-1} LWE) GMI GPROF precipitation rates (May 2014-December 2022) in (a-b) DJF and (c-d) JJA during AR and No AR events in the North Pacific. This figure is created using the variables "AR_flag" and "surface_precip" in the merged dataset.

Figures 7 and 8 show the DJF and JJA, gridded conditional mean (≥ 0.1 mm h^{-1} LWE) GMI GPROF precipitation rates in the North Atlantic and North Pacific, respectively, from the merged dataset. Precipitation rates are generally higher when ARs are present (Fig. 7a, c and Fig. 8a, c). The mean precipitation rate when an AR is present in the North Atlantic is 0.72 (0.78) mm h^{-1} in DJF (JJA) and in the North Pacific, is 0.70 (0.81) mm h^{-1} in DJF (JJA). Alternatively, precipitation rates are lower when no AR is present (Fig. 7b, d and Fig. 8b, d), with a basin-wide mean precipitation rate in the North Atlantic of 0.36 (0.51) mm h^{-1} in DJF (JJA) and in the North Pacific of 0.31 (0.49) mm h^{-1} in DJF (JJA). JJA precipitation rates (Fig. 7c-d and Fig. 8c-d) are generally higher than DJF precipitation rates (Fig. 7a-b and Fig. 8a-b) for both coincident AR and .

In DJF, precipitation rates are highest in the southeast region of both basins, and low in the northwest region. For example, in the North Atlantic (Fig. 7a-b), precipitation rates are lower (<

422 0.5 mm h^{-1}) north and west of the North Atlantic storm track. There is a similar pattern in the
423 North Pacific (Fig. 8a-b), where precipitation rates are lower (< 0.25 mm h^{-1}) north and west of
424 the Pacific storm track (Zhu & Newell, 1998; Guan & Waliser, 2015), with the exception of
425 higher rates in the Sea of Okhotsk (Fig. 8a-b) for both AR and non-AR scenarios. JJA
426 precipitation rates do not show a similar pattern along the storm tracks for either basin. In both
427 the Atlantic (Fig. 7c-d) and Pacific basins (Fig. 8c-d) during JJA, mean rates are highest (≥ 1.0
428 mm h-1) at lower latitudes (45 - 50ºN) and when an AR is present. Mean rates exceed 2 mm h^{-1}
429 in the southwest portion of both basins during JJA AR events (Fig. 7c, 8c).
430
431

DJF	**≥ 0.1 mm h^{-1}**		**≥ 0.5 mm h^{-1}**		**≥ 1.0 mm h^{-1}**	
Pacific	**AR**	**No AR**	**AR**	**No AR**	**AR**	**No AR**
45°-50°N	39.1	60.9	63.2	36.8	68.0	32.0
50°-55°N	45.2	54.8	70.5	29.5	73.1	26.9
55°-60°N	48.8	51.2	78.6	21.4	81.2	18.8
60°-65°N	52.3	47.7	93.3	6.68	96.0	4.01
45°-65°N	44.2	55.8	69.6	30.4	72.5	27.5
DJF	**≥ 0.1 mm h^{-1}**		**≥ 0.5 mm h^{-1}**		**≥ 1.0 mm h^{-1}**	
Atlantic	**AR**	**No AR**	**AR**	**No AR**	**AR**	**No AR**
45°-50°N	31.3	68.7	44.4	55.6	49.9	50.1
50°-55°N	29.2	70.8	48.9	51.1	54.7	45.3
55°-60°N	26.0	74.0	50.9	49.1	58.8	41.2

60°-65°N	28.6	71.4	57.1	42.9	65.1	34.9
45°-65°N	28.3	71.7	51.2	48.8	57.8	42.2

Table 2: Percentage of GMI footprints in DJF (May 2014-December 2022) with GMI GPROF precipitation rates (LWE) exceeding a minimum threshold (per 5° latitude bands: 45°-50°N, 50°-55°N, etc.) and North Pacific (top portion) and North Atlantic (bottom portion) basins south of 65°N (over ocean only). Percentages categorized by both the presence of an AR and the minimum precipitation rate.

JJA	**≥ 0.1 mm h^{-1}**		**≥ 0.5 mm h^{-1}**		**≥ 1.0 mm h^{-1}**	
Pacific	**AR**	**No AR**	**AR**	**No AR**	**AR**	**No AR**
45°-50°N	39.4	60.6	51.8	48.2	55.1	44.9
50°-55°N	39.7	60.3	54.0	46.0	57.3	42.7
55°-60°N	42.2	57.8	55.7	44.3	60.2	39.8
60°-65°N	43.6	56.4	55.1	44.9	59.1	40.9
45°-65°N	40.7	59.3	53.8	46.2	57.4	42.6
JJA	**≥ 0.1 mm h^{-1}**		**≥ 0.5 mm h^{-1}**		**≥ 1.0 mm h^{-1}**	
Atlantic	**AR**	**No AR**	**AR**	**No AR**	**AR**	**No AR**
45°-50°N	33.0	67.0	39.6	60.4	41.8	58.2
50°-55°N	33.0	67.0	42.7	57.3	46.3	53.7

55°-60°N	33.2	66.8	45.5	54.5	50.1	49.9
60°-65°N	36.8	63.2	52.4	47.6	57.8	42.2
45°-65°N	34.6	65.4	46.7	53.3	50.7	49.3

Table 3: Percentage of GMI footprints in JJA (May 2014-December 2022) with GMI GPROF precipitation rates (LWE) exceeding a minimum threshold (per 5° latitude bands: 45°-50°N, 50°-55°N, etc.) and North Pacific (top portion) and North Atlantic (bottom portion) basins south of 65°N (over ocean only). Percentages categorized by both the presence of an AR and the minimum precipitation rate.

Tables 2 and 3 list the percentage of GMI observations in DJF and JJA, respectively, filtered by minimum gridded GMI GPROF precipitation threshold (≥0.1, 0.5, and 1.0 mm h^{-1}), presence of an AR, and latitudinal boundaries (5° latitudinal increments and 45-65° over ocean only). In both the North Atlantic and North Pacific basins (45°-65°N), high precipitation rates are most often coincident with ARs, and low rates with no AR. In DJF, higher rates are more likely to be associated with ARs than during JJA. This is most apparent in the North Pacific basin, where 72.5% of high precipitation rates (≥ 1.0 mm h^{-1}) in DJF occur during an AR event. The percentage of AR-coincident high precipitation rates also increases as a function of latitude (poleward) in both basins, in agreement with the findings of Nash et al. (2018). The exception is that in JJA in the North Pacific basin, there is a slight decrease from 55°-60°N to 60°-65°N. One factor that may account for this is that there are fewer GMI footprints in the North Pacific due to the higher concentration of land surface grid boxes in the basin. Additionally, all JJA scenarios have more footprints than DJF as there are 2 months more data included in the 2014-2022 dataset (January and February 2014 pre-date GPM-CO) as well as reduced sea ice coverage (and therefore more over-ocean footprints) in JJA.

5 Example Application of Merged Dataset

To demonstrate a scientific application of this merged dataset, we examine the ERA5 T2M and total column water vapor (also known as TPW) data products during precipitating (threshold of 'surface_precip' ≥ 0.1 mm h^{-1}) AR and No AR conditions ('AR_flag' = 1, and 0, respectively). The GPROF algorithm estimates precipitation rates in conjunction with an *a priori* database that includes GANAL T2M and TPW, values both of which may be impacted by the presence of an AR. Histograms of T2M and TPW for the North Atlantic (Fig. 9) and North Pacific (Fig. 10) can be directly compared to the ocean surface type histogram in Fig. 8.2 of Randel et al. (2020) representing the environmental conditions within the GPROF *a priori* database.

The corresponding histograms between the two basins (Fig. 9 and Fig. 10) further explore the seasonality and AR presence during these environmental conditions. The composite of all 4 panels within each figure would closely resemble Fig. 8.2 in Randel et al. (2020), indicating that precipitating AR events are represented in the GPROF *a priori* database. There are more instances of precipitation at lower T2M and TPW values in DJF (Fig. 9a-b and Fig. 10a-b) than in JJA, and more instances of precipitation at higher T2M and TPW values in JJA (Fig. 9c-d and Fig. 10c-d). This corresponds to the colder, drier conditions in DJF and relatively warm, more moist conditions in JJA. Most retrieved precipitation in DJF occurs when the atmospheric water vapor content is low (< 20 mm), but at or above-freezing near-surface temperatures (T2M between 270 and 280 K). Retrieved precipitation in JJA occurs at a wide range of atmospheric moisture content (TPW between 10 and 65 mm) but most precipitation occurs at warm temperatures (T2M between 280 and 290 K).

The differences between T2M and TPW during precipitating AR versus No AR events are more subtle than the differences between seasons. As expected, the environment is often warmer and more moist during precipitation with ARs present (Fig. 9a, c and Fig. 10a, c) than when no AR is present (Fig. 9b, d and Fig. 10b, d). Precipitation is most frequent during No AR conditions and in DJF, can occur during very cold (T2M < 270 K) and dry (TPW < 5 mm) conditions (Fig. 9b and 10b). Further, Fig. 9 and 10 demonstrate the use of T2M and TPW as a good choice of constraints for GPROF. This merged dataset thus provides insight on the ability to examine retrieval performance and characteristics as a function of the environment, which is critical information for algorithm developers.

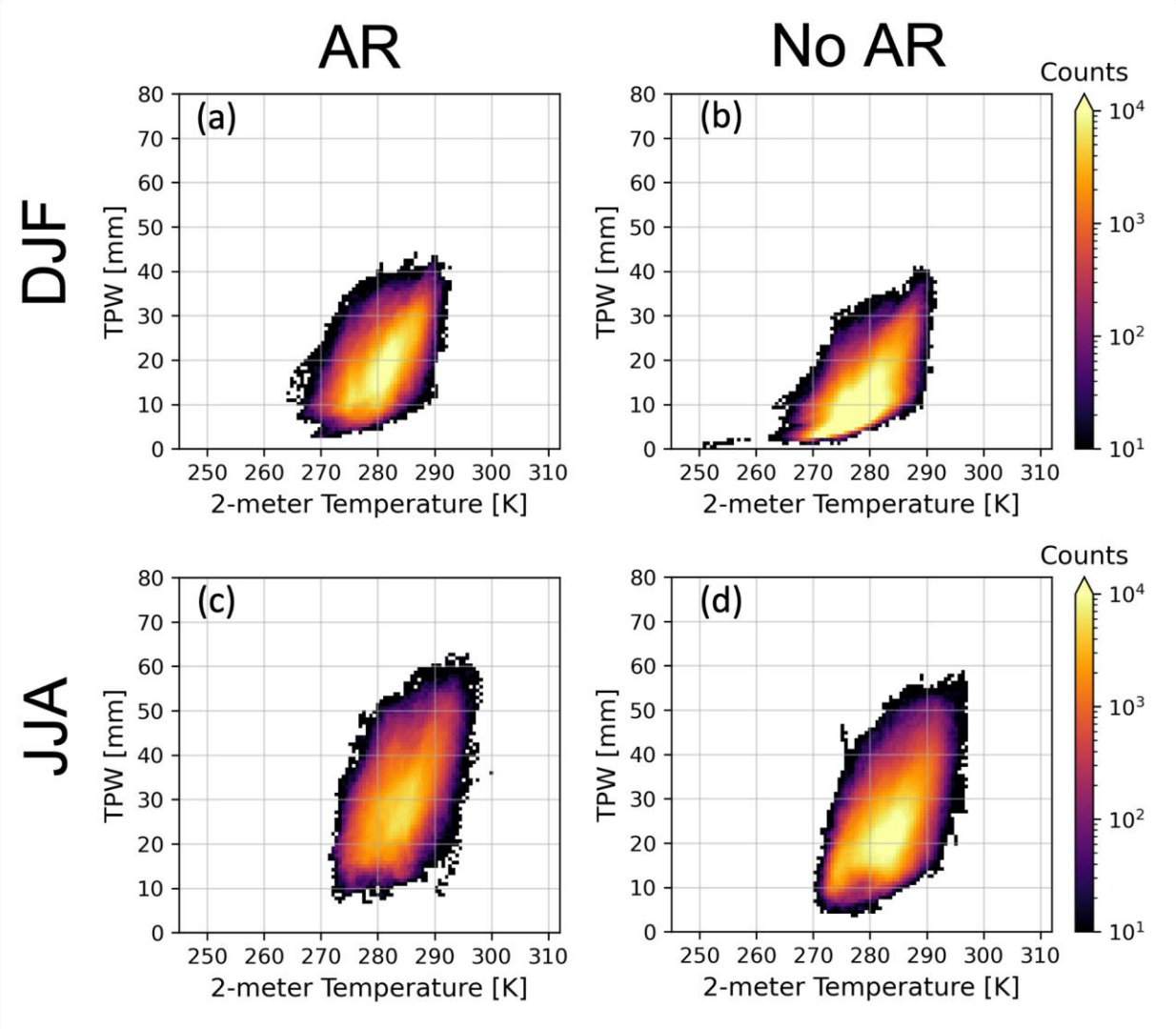

Figure 9: 2D Histograms of ERA5 T2M and total column water vapor (i.e., TPW) in the North Atlantic when matched gridded GMI GPROF precipitation rate ≥ 0.1 mm h^{-1} LWE (May 2014-December 2022).

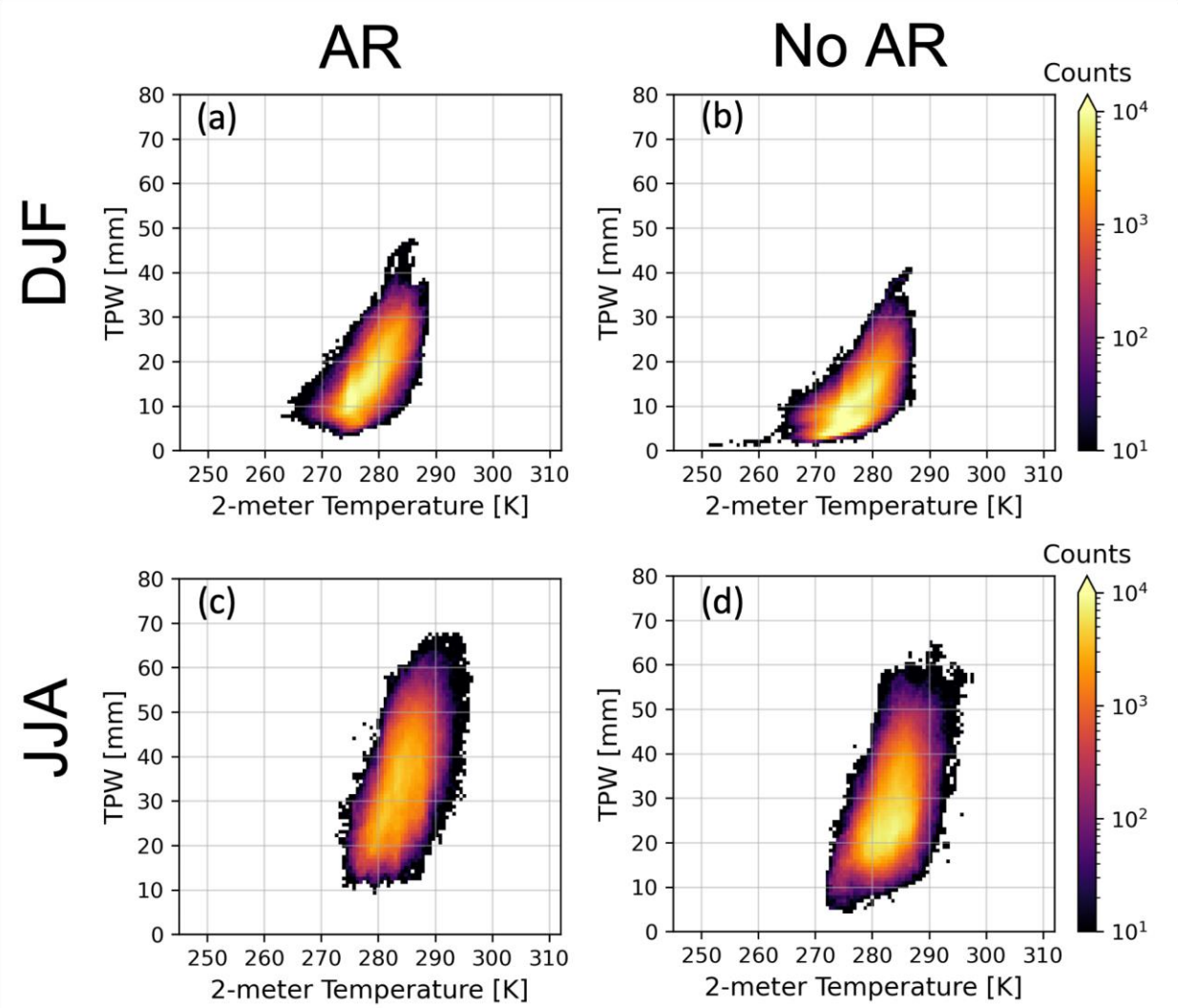

Figure 10: 2D Histograms of ERA5 T2M and total column water vapor (i.e., TPW) in the North Pacific when matched gridded GMI GPROF precipitation rate ≥ 0.1 mm h^{-1} LWE (May 2014-December 2022).

6 Summary and Conclusions

This paper presents a new dataset of coincident gridded GPM Core Observatory data products and M18 (Mattingly et al. 2018) ARs in the North Atlantic and Pacific sectors (45ºN to 68ºN) to provide the scientific community with a spaceborne perspective of AR effects on high-latitude precipitation. Matching an irregular grid of GPM-CO data in time and space to gridded, reanalysis-derived M18 ARs can be computationally challenging, and we therefore created this dataset to contribute to future AR research. We provide this dataset in monthly files separated by basin (‘atlantic’ vs ‘pacific’) for the duration of the GPM-CO’s life up to 2023 (March 2014 to

December 2022; with annual updates as new GMI and MERRA-2 data products become available).

The GPM-CO data merged with M18 ARs in this product are GMI Goddard Profiling (GPROF) version 7 precipitation estimates and version 8.2 of the Remote Sensing Systems (RSS) water vapor product, both derived from the GPM-CO microwave radiometer observations. We use a common grid of 0.25° × 0.25° for all data and assign each timestep as the median time of the GPM-CO overpass through the respective basin (North Atlantic or North Pacific). We show an example of a GPM-CO overpass (RSS water vapor and GMI GPROF precipitation) coincident with an M18 AR before and after gridding for the merged dataset. We then analyze the spatial patterns of precipitation and water vapor during AR and No AR events in both the North Atlantic and North Pacific basins. During an AR (No AR) event, GMI GPROF precipitation rates are higher (lower).

Finally, we apply the merged GPM-AR dataset to ERA5 T2M and total column water vapor (also known as TPW) data to compare environmental conditions during precipitation events depending on season, basin, and AR presence. We confirm that precipitation collocated with ARs is more intense and more likely to occur in warmer, more moist environments than when no AR is present. The GMI GPROF algorithm searches an *a priori* database containing GANAL T2M and TPW data (Randel et al., 2020) to estimate precipitation rate, and so the distinct histograms reflect the different environmental conditions (temperature and water vapor content) present. Further, differences between AR and No AR cases indicate that the GMI GPROF algorithm indirectly accounts for the presence of an AR when estimating precipitation rate.

Acknowledgement

This work was funded by the NASA Precipitation Measurement Mission Science Team Grants 80NSSC19K0712 and 80NSSC22K1315. The atmospheric river dataset is created using NASA's MERRA-2 reanalysis dataset (Gelaro et al., 2017), detailed in Mattingly et al. (2018).

Data Availability:

The merged dataset is available via Deep Blue Data (Mateling et al., 2023)
Appendix A details the netCDF contents for the merged dataset.

The M18 AR identification algorithm (version 2) code is available via Github (Mattingly, 2023).

The code to grid GPROF precipitation and merge with ARs is available via Github (Mateling, 2024).

The 2A GMI GPROF product (GPM_2AGPROFGPMGMI) was last accessed from the Goddard Earth Sciences (GES) Data and Information Services Center (DISC) in May 2023 (Kummerow 2022). GMI atmospheric water vapor data are produced by Remote Sensing Systems and sponsored by NASA Earth Science funding and are available at www.remss.com.

References

Baggett, C. F., Barnes, E. A., Maloney, E. D., & Mundhenk, B. D. (2017). Advancing atmospheric river forecasts into subseasonal-to-seasonal time scales. *Geophysical Research Letters*, *44*(14), 7528-7536. https://doi.org/10.1002/2017GL074434

Blackmon, M. L. (1976). A climatological spectral study of the 500 mb geopotential height of the Northern Hemisphere. *Journal of the Atmospheric Sciences*, *33*(8), 1607-1623.https://doi.org/10.1175/1520-0469(1976)033<1607:ACSSOT>2.0.CO;2

Cann, M. D., & Friedrich, K. (2020). The role of moisture pathways on snowfall amount and distribution in the Payette Mountains of Idaho. *Monthly Weather Review*, *148*(5), 2033-2048. https://doi.org/10.1175/MWR-D-19-0350.1

Cannon, F., Cordeira, J. M., Hecht, C. W., Norris, J. R., Michaelis, A., Demirdjian, R., & Ralph, F. M. (2020). GPM Satellite radar observations of precipitation mechanisms in atmospheric rivers. Monthly Weather Review, 148(4), 1449–1463. https://doi.org/10.1175/MWR-D-19-0278.1

Cannon, F., Ralph, F. M., Wilson, A. M., & Lettenmaier, D. P. (2017). GPM satellite radar measurements of precipitation and freezing level in atmospheric rivers: Comparison with ground-based radars and reanalyses. *Journal of Geophysical Research: Atmospheres*, *122*(23), 12-747. https://doi.org/10.1002/2017JD027355

Draper, D. W., D. Newell, F. J. Wentz, S. Krimchansky, and G. M. Skofronick-Jackson, 2015: The Global Precipitation Measurement (GPM) Microwave Imager (GMI): Instrument overview and early on-orbit performance. IEEE Journal of Selected Topics in Applied Earth Observations and Remote Sensing. doi:10.1109/JSTARS.2015.2403303.

Euronews.com (2016), Storm Urd lashes Scandinavian coast, Available from: https://www.euronews.com/2016/12/27/storm-urd-lashes-scandinavian-coast (Accessed 1 September 2023)

Gelaro, R., and Coauthors, 2017: The Modern-Era Retrospective Analysis for Research and Applications, Version 2 (MERRA-2). J. Climate, 30, 5419–5454, https://doi.org/10.1175/JCLI-D-16-0758.1.

Gimeno, L., Nieto, R., Vázquez, M., & Lavers, D. A. (2014). Atmospheric rivers: A mini-review. *Frontiers in Earth Science*, *2*, 2. https://doi.org/10.3389/feart.2014.00002

Goldenson, N., Leung, L. R., Bitz, C. M., & Blanchard-Wrigglesworth, E. (2018). Influence of atmospheric rivers on mountain snowpack in the western United States. *Journal of Climate*, 31(24), 9921–9940. https://doi.org/10.1175/JCLI-D-18-0268.1

Grecu, M., W. S. Olson, S. J. Munchak, S. Ringerud, L. Liao, Z. Haddad, B. L. Kelley, and S. F. McLaughlin, 2016: The GPM Combined Algorithm. J. Atmos. Oceanic Technol., 33, 2225–2245, https://doi.org/10.1175/JTECH-D-16-0019.1.

Guan, B., Molotch, N. P., Waliser, D. E., Fetzer, E. J., & Neiman, P. J. (2010). Extreme snowfall events linked to atmospheric rivers and surface air temperature via satellite measurements. *Geophysical Research Letters*, 37(20), L20401. https://doi.org/10.1029/2010GL044696

Guan, B., and D. E. Waliser (2015), Detection of atmospheric rivers: Evaluation and application of an algorithm for global studies, J. Geophys. Res. Atmos., 120, 12,514–12,535, doi:10.1002/2015JD024257.

Guan, B., Waliser, D. E., Ralph, F. M., Fetzer, E. J., & Neiman, P. J. (2016). Hydrometeorological characteristics of rain-on-snow events associated with atmospheric rivers. *Geophysical Research Letters*, 43, 2964–2973. https://doi.org/10.1002/2016GL067978

Hoskins, B. J., & Hodges, K. I. (2019a). The annual cycle of Northern Hemisphere storm tracks. Part I: Seasons. *Journal of Climate*, *32*(6), 1743-1760. https://doi.org/10.1175/JCLI-D-17-0870.1

Hoskins, B. J., & Hodges, K. I. (2019b). The annual cycle of Northern Hemisphere storm tracks. Part II: Regional detail. *Journal of Climate*, *32*(6), 1761-1775. https://doi.org/10.1175/JCLI-D-17-0871.1

Hoskins, B. J., & Valdes, P. J. (1990). On the existence of storm-tracks. *Journal of Atmospheric Sciences*, *47*(15), 1854-1864. https://doi.org/10.1175/1520-0469(1990)047<1854:OTEOST>2.0.CO;2

Hou, A. Y., Kakar, R. K., Neeck, S., Azarbarzin, A. A., Kummerow, C. D., Kojima, M., ... & Iguchi, T. (2014). The global precipitation measurement mission. *Bulletin of the American Meteorological Society*, *95*(5), 701-722. https://doi.org/10.1175/BAMS-D-13-00164.1

Kim, J., Waliser, D. E., Neiman, P. J., Guan, B., Ryoo, J. M., & Wick, G. A. (2013). Effects of atmospheric river landfalls on the cold season precipitation in California. Climate Dynamics, 40, 465–474. https://doi.org/10.1007/s00382-012-1322-3

Kojima, M., Miura, T., Furukawa, K., Hyakusoku, Y., Ishikiri, T., Kai, H., ... & Nakagawa, K. (2012). Dual-frequency precipitation radar (DPR) development on the global precipitation measurement (GPM) core observatory. In earth observing missions and sensors: development, implementation, and characterization II (Vol. 8528, pp. 234-243). SPIE. https://doi.org/10.1117/12.976823

Kummerow, C. (2022), GPM GMI (GPROF) Radiometer Precipitation Profiling L2A 1.5 hours 13 km V07, Greenbelt, MD, Goddard Earth Sciences Data and Information Services Center (GES DISC), Accessed: *May 2023*, 10.5067/GPM/GMI/GPM/GPROF/2A/07

Kummerow, C. D., Randel, D. L., Kulie, M., Wang, N. Y., Ferraro, R., Joseph Munchak, S., & Petkovic, V. (2015). The evolution of the Goddard profiling algorithm to a fully parametric scheme. *Journal of atmospheric and oceanic technology*, *32*(12), 2265-2280. https://doi.org/10.1175/JTECH-D-15-0039.1

Lavers, D. A., & Villarini, G. (2013). Atmospheric rivers and flooding over the central United States. *Journal of Climate*, 26(20), 7829–7836. https://doi.org/10.1175/JCLI-D-13-00212.1

Ma, Y., Hu, Z., Xie, Z., Ma, W., Wang, B., Chen, X., ... & Wang, Z. (2020). A long-term (2005–2016) dataset of hourly integrated land–atmosphere interaction observations on the Tibetan Plateau. *Earth System Science Data*, *12*(4), 2937-2957. https://doi.org/10.5194/essd-12-2937-2020

Mateling, M., (2024). Code to grid GMI GPROF precipitation data and merge with an Atmospheric River Dataset (Version 1) [Software]. Github. https://github.com/mmateling/grid_sat_data

Mateling, M. E., Pettersen, C., Kulie, M. S., Mattingly, K. S., Henderson, S. A., & L'Ecuyer, T. S. (2021). The influence of atmospheric rivers on cold-season precipitation in the Upper Great Lakes region. Journal of Geophysical Research: Atmospheres, 126, e2021JD034754. https://doi.org/10.1029/2021JD034754

669 Mateling, M., Pettersen, C., Mattingly, K., & Ringerud, S. (2023). Merged and Gridded GPM
670 and Atmospheric River Data Product (Version 1) [Dataset]. Deep Blue Data.
671 https://doi.org/10.7302/7t62-s085
672
673 Mattingly, K. (2018). AR Algorithm (Version 2) [Software]. Github.
674 https://github.com/ksmattingly/AR_alg_v2
675
676 Mattingly, K. S., Mote, T. L., & Fettweis, X. (2018). Atmospheric river impacts on Greenland
677 Ice Sheet surface mass balance. *Journal of Geophysical Research: Atmospheres*, *123*(16), 8538-
678 8560. https://doi.org/10.1029/2018JD028714
679
680 Mattingly, K. S., Mote, T. L., Fettweis, X., Van As, D., Van Tricht, K., Lhermitte, S., ... &
681 Fausto, R. S. (2020). Strong summer atmospheric rivers trigger Greenland Ice Sheet melt
682 through spatially varying surface energy balance and cloud regimes. *Journal of Climate*, *33*(16),
683 6809-6832. 10.1126/sciadv.abc2695
684
685 Mattingly, K. S., Turton, J. V., Wille, J. D., Noël, B., Fettweis, X., Rennermalm, Å. K., & Mote,
686 T. L. (2023). Increasing extreme melt in northeast Greenland linked to foehn winds and
687 atmospheric rivers. Nature Communications, 14(1), 1743. https://doi.org/10.1038/s41467-023-
688 37434-8
689
690 Mattingly, K. S., Ramseyer, C. A., Rosen, J. J., Mote, T. L., & Muthyala, R. (2016). Increasing
691 water vapor transport to the Greenland Ice Sheet revealed using self-organizing maps.
692 *Geophysical Research Letters*, *43*(17), 9250-9258. https://doi.org/10.1002/2016GL070424
693
694 Meissner, T., F. J. Wentz, and D. Draper, 2012: GMI Calibration Algorithm and Analysis
695 Theoretical Basis Document, Remote Sensing Systems, Santa Rosa, CA, report number 041912,
696 124 pp.
697
698 Nash, D., Waliser, D., Guan, B., Ye, H., & Ralph, F. M. (2018). The role of atmospheric rivers in
699 extratropical and polar hydroclimate. *Journal of Geophysical Research: Atmospheres*, 123,
700 6804–6821. https://doi.org/10.1029/ 2017JD028130
701
702 Passive Microwave Algorithm Team Facility: GLOBAL PRECIPITATION MEASUREMENT
703 (GPM) MISSION, NASA, https://gpm.nasa.gov/sites/default/files/2022-
704 06/ATBD_GPM_V7_GPROF.pdf, last access: July 2023.
705
706 Prein, A. F., & Heymsfield, A. J. (2020). Increased melting level height impacts surface
707 precipitation phase and intensity. *Nature Climate Change*, *10*(8), 771-776.
708 https://doi.org/10.1038/s41558-020-0825-x

Ralph, F. M., Cannon, F., Tallapragada, V., Davis, C. A., Doyle, J. D., Pappenberger, F., ... & Delle Monache, L. (2020). West Coast forecast challenges and development of atmospheric river reconnaissance. *Bulletin of the American Meteorological Society*, *101*(8), E1357-E1377. https://doi.org/10.1175/BAMS-D-19-0183.1

Ralph, F. M., Dettinger, M. D., Cairns, M. M., Galarneau, T. J., & Eylander, J. (2018). Defining "atmospheric river": How the Glossary of Meteorology helped resolve a debate. *Bulletin of the American Meteorological Society*, *99*(4), 837-839. https://doi.org/10.1175/BAMS-D-17-0157.1

Ralph, F. M., P. J. Neiman, and G. A. Wick, 2004: Satellite and CALJET Aircraft Observations of Atmospheric Rivers over the Eastern North Pacific Ocean during the Winter of 1997/98. Mon. Wea. Rev., 132, 1721–1745, https://doi.org/10.1175/1520-0493(2004)132<1721:SACAOO>2.0.CO;2.

Randel, D. L., Kummerow, C. D., & Ringerud, S. (2020). The Goddard Profiling (GPROF) precipitation retrieval algorithm. *Satellite Precipitation Measurement: Volume 1*, 141-152. https://doi.org/10.1007/978-3-030-24568-9_8

Rutz, J. J., Shields, C. A., Lora, J. M., Payne, A. E., Guan, B., Ullrich, P., et al. (2019). The atmospheric river tracking method intercomparison project (ARTMIP): quantifying uncertainties in atmospheric river climatology. Journal of Geophysical Research: Atmospheres, 2019; 124: 13777–13802. https://doi.org/10.1029/2019JD030936

Shields, C. A., Rutz, J. J., Leung, L. Y., Ralph, F. M., Wehner, M., Kawzenuk, B., ... & Nguyen, P. (2018). Atmospheric river tracking method intercomparison project (ARTMIP): project goals and experimental design. *Geoscientific Model Development*, *11*(6), 2455-2474. https://doi.org/10.5194/gmd-11-2455-2018

Sims, E. M., and G. Liu, 2015: A Parameterization of the Probability of Snow–Rain Transition. J. Hydrometeor., 16, 1466–1477, https://doi.org/10.1175/JHM-D-14-0211.1.

Skofronick-Jackson, G.; Kirschbaum, D.; Petersen, W.; Huffman, G.; Kidd, C.; Stocker, E.; Kakar, R. The Global Precipitation Measurement (GPM) mission's scientific achievements and societal contributions: Reviewing four years of advanced rain and snow observations. Q. J. R. Meteorol. Soc. 2018, 144, 27–48.

Skofronick-Jackson, G., M. Kulie, L. Milani, S. J. Munchak, N. B. Wood, and V. Levizzani, 2019: Satellite Estimation of Falling Snow: A Global Precipitation Measurement (GPM) Core

Observatory Perspective. J. Appl. Meteor. Climatol., 58, 1429–1448, https://doi.org/10.1175/JAMC-D-18-0124.1.

Skofronick-Jackson, G., Petersen, W. A., Berg, W., Kidd, C., Stocker, E. F., Kirschbaum, D. B., ... & Wilheit, T. (2017). The Global Precipitation Measurement (GPM) mission for science and society. Bulletin of the American Meteorological Society, 98(8), 1679-1695. https://doi.org/10.1175/BAMS-D-15-00306.1

Slinskey, E. A., Loikith, P. C., Waliser, D. E., Guan, B., & Martin, A. (2020). A climatology of atmospheric rivers and associated precipitation for the seven U.S. National Climate Assessment Regions. *Journal of Hydrometeorology*, 21, 2439–2456. https://doi.org/10.1175/JHM-D-20-0039.s1

Zhu, Y., & Newell, R. E. (1998). A proposed algorithm for moisture fluxes from atmospheric rivers. *Monthly weather review*, *126*(3), 725-735. https://doi.org/10.1175/1520-0493(1998)126<0725:APAFMF>2.0.CO;2

Wentz, F.J., T. Meissner, J. Scott, K.A. Hilburn, 2015: Remote Sensing Systems GPM GMI Daily Environmental Suite on 0.25 deg grid, Version 8.2. Remote Sensing Systems, Santa Rosa, CA. Available online at www.remss.com/missions/gmi. [Accessed 16 Sep 2022].

Appendices

Appendix A

Table 1

The merged dataset is available in netCDF-4 format for ease of sharing and compatibility within the academic community. The monthly files are compressed into year and basin: either the North Atlantic (NA) or the North Pacific (NP) (e.g., NA_2014) and zipped. The files have the basin name indicated and are by year and month (e.g., gridded_atlantic_YYYYMM.nc). Each netCDF file contains the following variables:

Variable Name	Description	Dimensions	Units
time	Timestamp	(time)	YYYY-mm-dd HH:MM:SS

latitude	-	45 - 70° N(lat)	Degrees North
longitude	-	N Atlantic: 70° W - 10° E N Pacific: 140° E - 120° W (lon)	Degrees East
surface_precip	GPROF Surface Precipitation	(time, lat, lon)	mm h^{-1} LWE
surface_frozen	GPROF Frozen Precipitation	(time, lat, lon)	mm h^{-1} LWE
rain	GPROF Surface Precipitation (minus) GPROF Frozen Precipitation	(time, lat, lon)	mm h^{-1} LWE
temp_2m	GPROF 2-meter temperature	(time, lat, lon)	K
sfc_type_flag	Surface Type Flag: 0 = ocean, 1 = land, 2 = mixed	(time, lat, lon)	-
precip_flag	Precipitation Flag: 0 = No Precip, 1 = Surface Precip, 2 = Frozen Precip	(time, lat, lon)	-
AR_flag	Atmospheric River Flag: 0 = No AR, 1 = AR	(time, lat, lon)	-
RSS_wv	Remote Sensing Systems atmospheric vapor	(time, lat, lon)	mm
opass_counts	Overpass Counts	(lat, lon)	-
counts_pr_gr0	Counts of Precip > 0 mm h^{-1}	(lat, lon)	-
counts_pr_gr0p1	Counts of Precip ≥ 0.1 mm h^{-1}	(lat, lon)	-

counts_pr_gr0p5	Counts of Precip ≥ 0.5 mm h^{-1}	(lat, lon)	-
counts_pr_gr1	Counts of Precip ≥ 1.0 mm h^{-1}	(lat, lon)	-
counts_fzn_gr0	Counts of Frozen Precip > 0 mm h^{-1}	(lat, lon)	-
counts_fzn_gr0p1	Counts of Frozen Precip ≥ 0.1 mm h^{-1}	(lat, lon)	-
counts_fzn_gr0p5	Counts of Frozen Precip ≥ 0.5 mm h^{-1}	(lat, lon)	-
counts_fzn_gr1	Counts of Frozen Precip ≥ 1.0 mm h^{-1}	(lat, lon)	-
counts_rn_gr0	Counts of (Surface minus Frozen) Precip > 0 mm h^{-1}	(lat, lon)	-
counts_rn_gr0p1	Counts of (Surface minus Frozen) Precip ≥ 0.1 mm h^{-1}	(lat, lon)	-
counts_rn_gr0p5	Counts of (Surface minus Frozen) Precip ≥ 0.5 mm h^{-1}	(lat, lon)	-
counts_rn_gr1	Counts of (Surface minus Frozen) Precip ≥ 1.0 mm h^{-1}	(lat, lon)	-
AR_counts_pr_gr0	Counts of Precip > 0 mm h^{-1} during AR	(lat, lon)	-
AR_counts_pr_gr0p1	Counts of Precip ≥ 0.1 mm h^{-1} during AR	(lat, lon)	-
AR_counts_pr_gr0p5	Counts of Precip ≥ 0.5 mm h^{-1} during AR	(lat, lon)	-
AR_counts_pr_gr1	Counts of Precip ≥ 1.0 mm h^{-1} during AR	(lat, lon)	-
AR_counts_fzn_gr0	Counts of Frozen Precip > 0 mm h^{-1}	(lat, lon)	-

	during AR		
AR_counts_fzn_gr0p1	Counts of Frozen Precip ≥ 0.1 mm h^{-1} during AR	(lat, lon)	-
AR_counts_fzn_gr0p5	Counts of Frozen Precip ≥ 0.5 mm h^{-1} during AR	(lat, lon)	-
AR_counts_fzn_gr1	Counts of Frozen Precip ≥ 1.0 mm h^{-1} during AR	(lat, lon)	-
AR_counts_rn_gr0	Counts of (Surface minus Frozen) Precip > 0 mm h^{-1} during AR	(lat, lon)	-
AR_counts_rn_gr0p1	Counts of (Surface minus Frozen) Precip ≥ 0.1 mm h^{-1} during AR	(lat, lon)	-
AR_counts_rn_gr0p5	Counts of (Surface minus Frozen) Precip ≥ 0.5 mm h^{-1} during AR	(lat, lon)	-
AR_counts_rn_gr1	Counts of (Surface minus Frozen) Precip ≥ 1.0 mm h^{-1} during AR	(lat, lon)	-
noAR_counts_pr_gr0	Counts of Precip > 0 mm h^{-1} during No AR	(lat, lon)	-

Note. Files are separated into individual basins (North Atlantic or North Pacific) and each file contains one month of data. For example, the file containing the merged dataset for May 2014 in the North Atlantic is named, “atlantic_201405.nc.” The dimensions for this file are: timestep = 288 (number of overpasses through the North Atlantic basin during May 2014), latitude = 100, and longitude = 320. Precipitation rates are expressed as mm h-1 liquid water equivalent (LWE).

Figure 1.

GPM Footprint & M18 AR

Gridded GPM & AR

RSS Water Vapor

GPROF Precip Rate

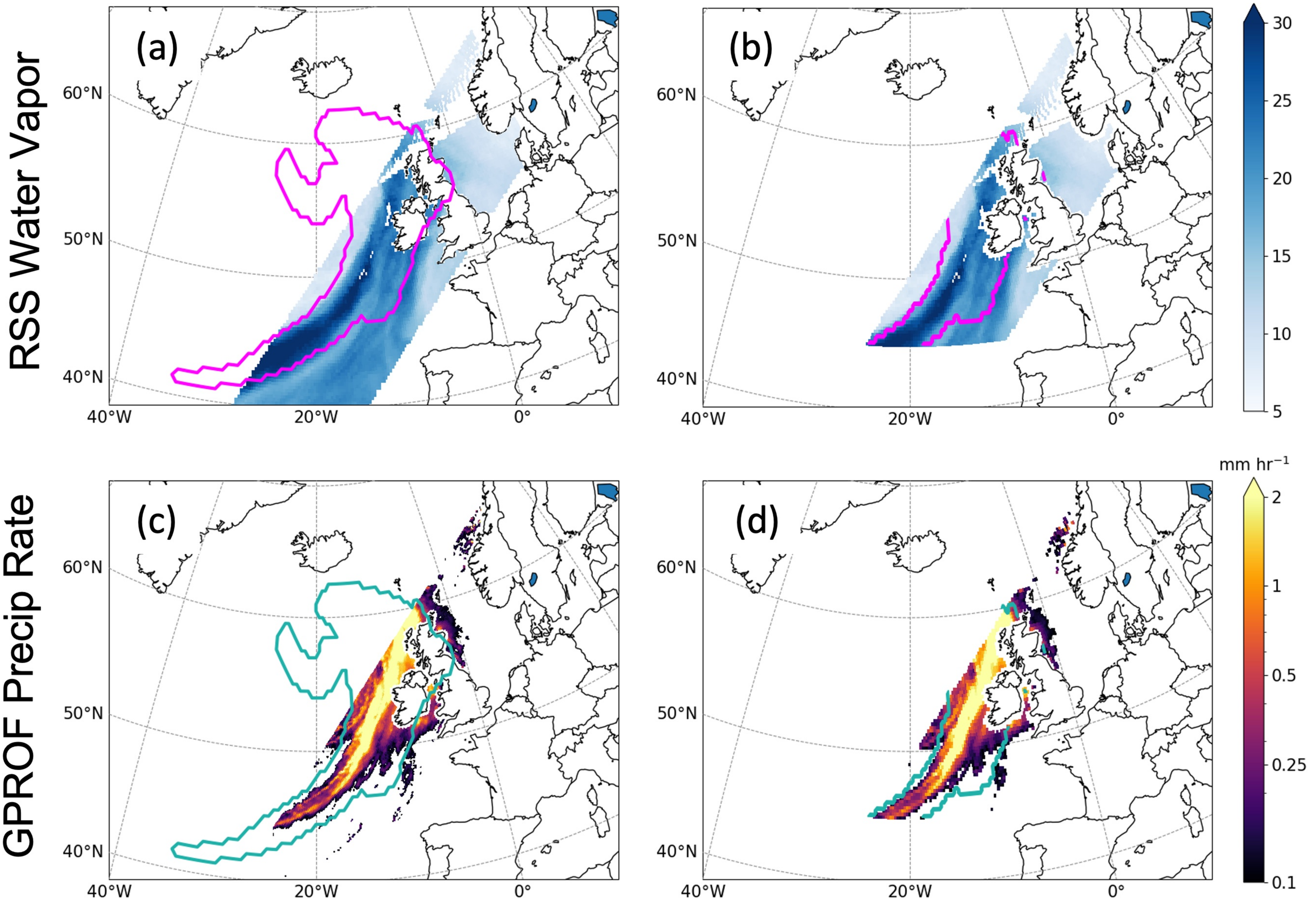

Figure 2.

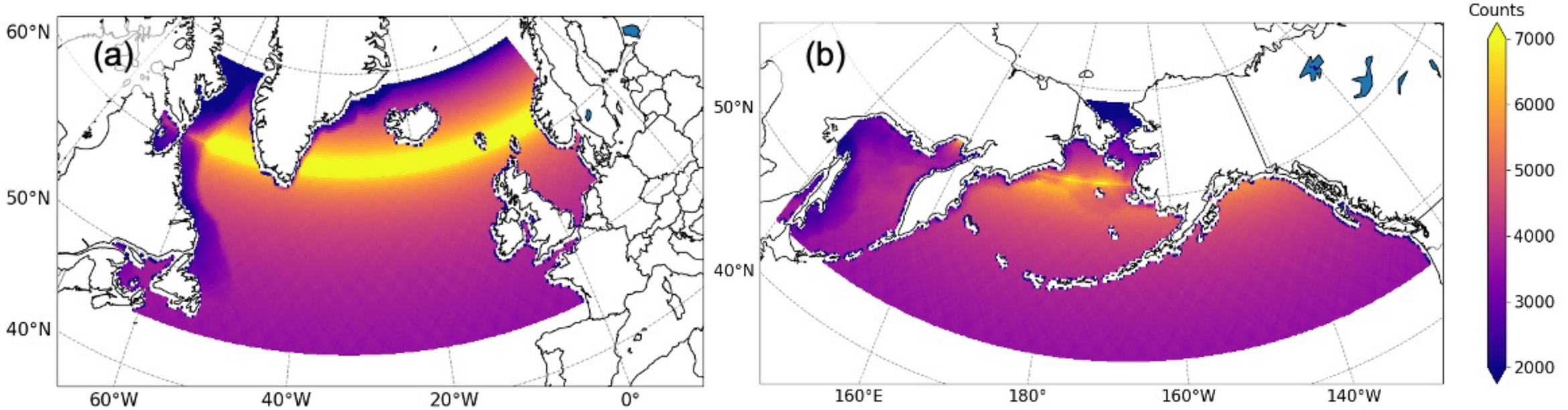
(a)
(b)
60°N
50°N
40°N
60°W
40°W
20°W
0°
50°N
40°N
160°E
180°
160°W
140°W
Counts
7000
6000
5000
4000
3000
2000

Figure 3.

DJF

JJA

North Atlantic

North Pacific

(a)

(b)

(c)

(d)

60°N

50°N

40°N

60°W

40°W

20°W

0°

160°E

180°

160°W

140°W

2

4

6

8

10

12

14

16

18

20

%

Figure 4.

AR

No AR

DJF

(a)

(b)

60°N

50°N

40°N

60°W

40°W

20°W

0°

5

10

15

20

25

mm

JJA

(c)

(d)

60°N

50°N

40°N

60°W

40°W

20°W

0°

10

15

20

25

30

35

40

mm

Figure 5.

AR

No AR

DJF

(a)

(b)

50°N

40°N

160°E 180° 160°W 140°W

160°E 180° 160°W 140°W

5 10 15 20 25

mm

JJA

(c)

(d)

50°N

40°N

160°E 180° 160°W 140°W

160°E 180° 160°W 140°W

10 15 20 25 30 35 40

mm

Figure 6.

North Atlantic

(a) DJF

(b) JJA

North Pacific

(c)

(d)

Counts

Precip [mm h^{-1}]

AR

No AR

Figure 7.

AR

No AR

DJF

JJA

(a)

(b)

(c)

(d)

60°N

50°N

40°N

60°W

40°W

20°W

0°

0.1

0.25

0.5

1

2

mm h^{-1}

Figure 8.

AR

No AR

DJF

JJA

(a)

(b)

(c)

(d)

50°N

40°N

160°E

180°

160°W

140°W

0.1

0.25

0.5

1

2

mm h^{-1}

Figure 9.

AR

No AR

DJF

JJA

(a)

(b)

(c)

(d)

TPW [mm]

2-meter Temperature [K]

Counts

10^4

10^3

10^2

10^1

Figure 10.

AR

No AR

DJF

JJA

(a)

(b)

(c)

(d)

TPW [mm]

2-meter Temperature [K]

Counts

10^4

10^3

10^2

10^1